PCCP

Accepted Manuscript

ROYAL SOCIETY OF CHEMISTRY

www.rsc.org/pccp

Physical Chemistry Chemical Physics

Cite this: DOI: 10.1039/c0xx00000x

www.rsc.org/xxxxxx

ARTICLE TYPE

S-doped mesoporous nanocomposite of $HTiNbO_5$ nanosheets and TiO_2 nanoparticles with an enhanced visible light photocatalytic activity

Chao Liu,[ab] Ruirui Han,[a] Hongmei Ji,[a] Tao Sun,[a] Jin Zhao,[a] Ningna Chen[a], Jing Chen,[c] Xuefeng Guo,[a] Wenhua Hou*[a] and Weiping Ding[a]

Received (in XXX, XXX) Xth XXXXXXXXX 20XX, Accepted Xth XXXXXXXXX 20XX
DOI: 10.1039/b000000x

S-doped mesoporous nanocomposite (S-TNT) of $HTiNbO_5$ nanosheets (NSs) and anatase TiO_2 nanoparticles (NPs) with exposed {101} facets, have been successfully synthesized by first mixing freeze-dried $HTiNbO_5$ NSs with titanium isopropoxide and then calcination with thiourea in air. The exposed anatase {101} facets can be acted as a possible reservoir of the photogenerated electrons, yielding a highly reactive surface for the reduction of O_2 to $O_2^{\bullet-}$. The partial substitution of Ti^{4+} by S^{6+} in the lattice of TiO_2 NPs leads to a charge imbalance in S-TNT and the formation of Ti−O−S bond. As a result, the formed cationic S-TNT is in favour of adsorbing hydroxide ions (OH^-_{ads}) and thus capturing the photo-induced holes to form hydroxyl radicals ($^{\bullet}OH$). Meanwhile, with the formation of Ti−O−S bond, partial electrons can be transferred from S to O atoms and hence the electron-deficient S atoms might capture photo-induced electrons. The surface-adsorbed SO_4^{2-} could also act as the efficient electron trapping center to promote the separation of charge carriers. In addition, the Ti^{3+} species due to the removal of oxygen atoms during calcination and the associated oxygen vacancy defects on the surface of S-TNT could act as hole and electron scavengers, respectively. Besides, the closely-contacted interface is formed between $HTiNbO_5$ NSs and anatase TiO_2 NPs due to the common features of TiO_6 octahedra in two components, resulting in a nanoscale heterojunction structure to speed up the separation rate of photogenerated charge carriers. The formation of a nano-heterojunction and the incorporation of Ti^{3+} and S dopants give rise to the visible and near-infrared light response of S-TNT. The combined effects greatly retard the charge recombination and improve the photocatalytic activity for the degradation of rhodamine B (RhB) and phenol solution under visible light irradiation. The corresponding photocatalytic mechanism was investigated *via* the active species capture experiments. The present work may provide an insight for the fabrication of delicate composite photocatalysts with an excellent performance.

Introduction

The growing concerns about environmental and energy crises have attracted more and more attention on solar energy utilization.[1-7] The effectiveness of solar-driven photocatalytic degradation of organic pollutants is determined to a great extent by the semiconductor's capability of absorbing visible and infrared light, as well as its ability to suppress the rapid combination of photogenerated electrons and holes.[8-10] As a "green" method, the semiconductor photocatalysis technique has triggered extensive research interest because it can eliminate most organic contaminants. Among those semiconductors, TiO_2 has been widely studied due to its low cost and toxicity, good chemical and thermal stability, exceptional optical and electronic properties, and high photoactivity.[11-14] However, two major limitations of TiO_2 photocatalyst are the poor response to the visible-light irradiation and the rapid recombination of photogenerated electron-hole pairs.

Layered compounds have grabbed appreciable attention due to their unique structure and electrical properties.[15-17] Particularly, layered materials could be exfoliated to prepare monolayer or few-layer 2D nanosheet materials.[18] A broad interest has been aroused as these 2D nanosheets have extraordinary properties and potential applications in the areas of electronics, catalysis, chemical and biological sensors, supercapacitors and energy storage.[19-22] Among those layered materials, $HTiNbO_5$ is a typical layered solid acid in which H^+ ions lie between $TiNbO_5^-$ layers built up from zigzag chains of edge-sharing MO_6 octahedra. However, like TiO_2, $HTiNbO_5$ itself has a relatively wide bandgap (3.32 eV),[23] showing some drawbacks such as a poor response to visible light and a high rate of electron–hole recombination.

During the past decade, some effective strategies such as doping, morphology control and heterojunction coupling have all been reported to improve the photocatalytic activity.[24-27] The addition of the controlled metal or nonmetal impurities have been employed to generate donor or acceptor states in the band gap. Besides impurity incorporation, self-doping that produces Ti^{3+} species in TiO_2 has also been demonstrated to increase optical absorption.[28,29] On the other hand, the construction of heterojunction photocatalysts by integrating different individual materials, can effectively speed up the separation rate of photogenerated charge carriers and thus enhance the photocatalytic activity for decomposing organic contaminants.[30,31] In addition, the morphology control, particularly in order to obtain the specifically exposed crystal facets, could separate the charge carriers and thus enhance the photocatalytic performance.[32,33] Therefore, it is reasonable to design novel photocatalysts through the integration of doping, heterojunction formation and morphology engineering strategies. For example, our group once reported that N- and S-doped $Na_2Ti_6O_{13}$@TiO_2 core-shell nanobelts showed an enhanced visible-light photocatalytic performance due to the combination effects of nonmetal doping, heterojunction formation and morphology engineering.[34,35]

Taking this design idea, here in this work, S-doped mesoporous nanocomposite of $HTiNbO_5$ NSs and TiO_2 NPs with exposed {101} facets has been synthesized *via* a simple exfoliation-reassembly-calcination method. The resulted nanocomposite exhibits an excellent photocatalytic activity in the degradation of RhB and phenol under visible-light irradiation. The structure, surface morphology and photocatalytic performance of the resultant samples have been studied and discussed in detail. Moreover, a possible photocatalytic mechanism is proposed based on the experimental results.

Experimental section

Synthesis of S-doped mesoporous TiO_2/$HTiNbO_5$ nanocomposite

Layered $KTiNbO_5$ was synthesized by heating a stoichiometric mixture of K_2CO_3, TiO_2 and Nb_2O_5 in molar ratios of 1:2:1 at 1100 °C for 24 h, according to the procedure described in the literature.[36] The protonated form $HTiNbO_5$ was obtained by the treatment of $KTiNbO_5$ with 5M HNO_3 aqueous solution at room temperature for 3 days. During the proton exchange reaction, the acidic solution was replaced with a fresh one every 24 h.

To prepare $HTiNbO_5$ NSs, the obtained $HTiNbO_5$ (1.0 g) was dispersed in 200 mL distilled water and then 10 wt% of tetrabutylammonium hydroxide (TBAOH) was added dropwise until the pH value reached 9-10. After stirring for 7 days, the supernatant solution containing $HTiNbO_5$ NSs (0.4 g/100 mL) was collected by means of a high-speed centrifugation (5000 rpm for 6 min). The resulted $HTiNbO_5$ NSs were freeze-dried and then re-dispersed in ethanol (20 mg/mL). For the sample of S-TNT, the loading amount of TiO_2 on the surface of $HTiNbO_5$ NSs is 86.1 wt%.

S-doped mesoporous TiO_2/$HTiNbO_5$ nanocomposite (denoted as S-TNT) was prepared by adding dropwise 10 mL titanium isopropoxide (Ti(O-*i*-Pr)$_4$) into the above suspension (50 mL) under stirring. After 2 h, the resultant suspension was transferred to a petri-dish and dried at room temperature to allow solvent evaporation. The resulted solid sample (1.0 g) was finely milled with thiourea (2.0 g) and then calcined in air at 450 °C for 2 h with a heating rate of 10 °C/min. After calcination treatment, the solid product was crushed, washed well with distilled water to remove likely residual thiourea precursors, and finally dried at 70 °C overnight. For comparison, S-doped $HTiNbO_5$ NSs (denoted as S-TN) was prepared *via* the similar process in which no Ti(O-*i*-Pr)$_4$ was added and freeze-dried $HTiNbO_5$ NSs were directly milled with thiourea. In addition, the corresponding undoped samples (denoted as TNT and TN) were also prepared through the respective process in which no thiourea was added.

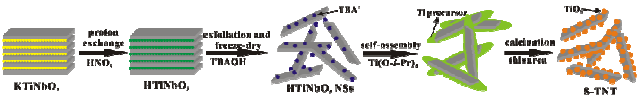

Fig. 1 A schematic illustration for the synthesis of S-doped nanocomposite of $HTiNbO_5$ NSs and TiO_2 NPs.

A schematic illustration for the formation process of S-doped mesoporous TiO_2/$HTiNbO_5$ nanocomposite is presented in Fig. 1. The protonated form $HTiNbO_5$ was obtained *via* the proton exchange reaction of $KTiNbO_5$ with HNO_3 aqueous solution, and then TBAOH was added to exfoliate $HTiNbO_5$ and thus obtain $HTiNbO_5$ NSs with the freeze-dry treatment. Upon reaction with Ti(O-*i*-Pr)$_4$, freeze-dried $HTiNbO_5$ NSs were covered with Ti precursor through a re-assembly process. Then, after mixing with thiourea and calcination in air, S-doped TiO_2/$HTiNbO_5$ nanocomposite, in which TiO_2 NPs were deposited on $HTiNbO_5$ NSs, was obtained.

Characterization

The morphology was investigated by transmission electron microscopy (TEM, JEOL JEM-200CX, operating at an accelerating voltage of 200 kV). For TEM observation, the samples were dispersed in ethanol by ultrasonic treatment and dropped onto carbon-coated copper grids. XRD patterns of the obtained samples were taken on a Philip-X'Pert X-ray diffractometer with a Cu Kα radiation (λ =1.5418 Å) and Ni filter at a scanning rate of 0.2 °/s in a 2θ range of 5~60°. The samples were pressed into a thin disk and fixed in a homemade quartz cell. X-ray photoelectron spectroscopic (XPS) analysis was carried out on an X-ray photoelectron spectrometer (Thermo Fisher Scientific, K-Alpha) equipped with a hemispherical electron analyzer (pass energy of 20 eV) and an Al Kα (*hv* =1486.6 eV) X-ray source. Electron paramagnetic resonance (EPR) measurement was conducted on a Bruker EMX-10/12 EPR spectrometer at room temperature. UV–vis diffuse reflectance spectra were obtained on a UV–vis spectrophotometer (Shimadzu, UV-2401) using $BaSO_4$ as reference. The Brunauer–Emmett–Teller (BET) specific surface area and Barrett–Joyner–Halenda (BJH) pore size distribution curve were obtained from N_2 adsorption and desorption isotherms determined at liquid nitrogen temperature (77 K) on a Micromeritics ASAP 2020 surface area and porosity analyzer. Samples were degassed at 573 K for 5 h prior to the measurement. The photoluminescence (PL) spectrum was recorded with a Varian Cary eclipse spectrometer with an excitation wavelength of 350 nm at room temperature. The binding energies (BE) were referenced to the adventitious C

1s peak (284.6 eV) which was used as an internal standard to take into account charging effects. A combination of Gaussian and Lorentzian functions was used to fit the curves.

Photocatalytic reaction tests

The visible light photocatalytic activity was evaluated by the degradation of RhB and phenol in aqueous solution. Firstly, 50 mg of catalyst was respectively suspended in RhB and phenol aqueous solution (1.0×10^{-5} mol/L) in the dark for more than 1 h, in order to gain the adsorption-desorption equilibrium. After the adsorption equilibrium, the catalyst was separated and re-dispersed in an aqueous solution of RhB or phenol (100 mL, 1.0×10^{-5}mol/L) in a beaker with a circulating water system to remove the thermal effect of light. Light from a 300 W Xe lamp, passed through a UV light filter film (to remove radiation with $\lambda<$ 420 nm), was focused onto the reaction cell. The optical power and power density were recorded on a CEL-NP2000 (see Table S1). When the light was turned on, at given time intervals, approximately 4 mL of the reaction suspension was sampled and separated by means of high-speed centrifugation. The filtrates were analyzed by recording the maximum absorbance at 664 and 269 nm in the UV-visible spectra of RhB and phenol, respectively. The degradation efficiency at time t was determined from the value of C_t/C_0, where C_0 is the initial concentration and C_t is the concentration of RhB at time t.

The recycling photocatalytic activity test was performed as follows. After the 1st run of the reaction, the catalyst was collected and cleaned for the next run. Similarly, 3rd, 4th and 5th runs were carried out.

The active species capture experiments were carried out to study the photocatalytic mechanism. Different radical scavengers such as silver nitrate ($AgNO_3$, 1 mmol/L), ethylenediaminetetraacetic acid disodium salt (EDTA, 1 mmol/L), *tert*-butyl alcohol (BuOH, 5 mmol/L) and p-benzoquinone (BZQ, 1 mmol/L) were added to the RhB aqueous solution, respectively. Then, the remaining experimental processes were similar to the above photocatalytic test.

Results and discussion

Morphology

Fig. 2 shows TEM and HRTEM images of $HTiNbO_5$ NSs and S-TNT. As shown in Fig. 2a, $HTiNbO_5$ NSs in colloidal solution can be clearly observed from TEM image. Compared with pure $HTiNbO_5$ NSs, S-TNT presents a TEM image of the composite material (Fig. 2b). It is visible that TiO_2 NPs are deposited on the surface of $HTiNbO_5$ NSs.

As shown in Fig. 2c, the HRTEM image of S-TNT also confirms that the composite material possesses a hybrid structure with anatase TiO_2 NPs deposited on the surface of $HTiNbO_5$ NSs. For anatase TiO_2 NPs with a size of ~3-10 nm, the well-resolved interplanar spacing is about ~0.35 nm. Considering the crystallographic symmetry of anatase, the dominant exposed facets can be identified as {101} planes, which were generally regarded as the most thermodynamically stable facets of anatase TiO_2.[32] It has been reported that the anatase TiO_2 nanocrystals with the reductive {101} facets acting as a possible reservoir of the photogenerated electrons, could provide a highly reactive

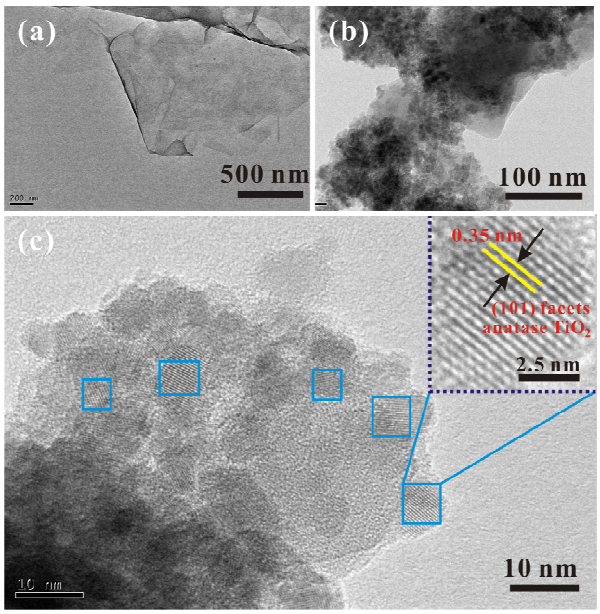

Fig. 2 EM images of $HTiNbO_5$ NSs and S-TNT. (a) TEM of $HTiNbO_5$ NSs, (b) TEM of S-TNT and (c) HRTEM of S-TNT.

surface for the reduction of O_2 to $O_2^{\bullet-}$ and thus promote the charge separation.[32, 34, 37] In addition, the HRTEM image of S-TNT also demonstrates the highly crystalline nature of both $HTiNbO_5$ and TiO_2 and a closely contacted interface between two components.

XRD analysis

The layered structure and crystallinity of the resulting samples were characterized by XRD. As shown in Fig. 3, the XRD pattern of the as-prepared $HTiNbO_5$ matches well with the published data (PDF, #75-2062).[38] According to the position of the characteristic (002) reflection of the layered structure, the interlayer distance of $HTiNbO_5$ is calculated to be 8.3 Å (2θ = 10.7°). After exfoliation, freeze-drying and calcination with thiourea, the characteristic (002) reflection is completely disappeared in the resulting S-TN and only three weak peaks at about 24.3°, 27.9° and 48.5° exist, indicating the collapse of the ordered layered structure and the formation of $HTiNbO_5$ NSs. Although other characteristic diffraction peaks of $HTiNbO_5$ are not obviously observed, it doesn't mean that $HTiNbO_5$ NSs are decomposed into other phases due to its highly thermal stability.[38] By comparison, when the freeze-dried $HTiNbO_5$ NSs were calcinated without the addition of thiourea, the resulted TN shows the similar XRD pattern with S-TN and only a slight decrease in intensities, indicating that the addition of thiourea plays an important role in stabilizing a better crystallinity of $HTiNbO_5$.[35]

After reaction of freeze-dried $HTiNbO_5$ NSs with $Ti(O\text{-}i\text{-}Pr)_4$ and then calcination with thiourea in air at 450 °C, the characteristic diffraction peaks of $HTiNbO_5$ fully disappear and only weak and broadened peaks of anatase TiO_2 appear in the obtained nanohybrid S-TNT, indicating a much poorer periodic layered structure than the original $HTiNbO_5$ and the fine hybridization of anatase TiO_2 NPs with $HTiNbO_5$ NSs. In addition, $HTiNbO_5$ NSs are fully covered with TiO_2 NPs and thus the characteristic diffraction peaks of layered $HTiNbO_5$ are not

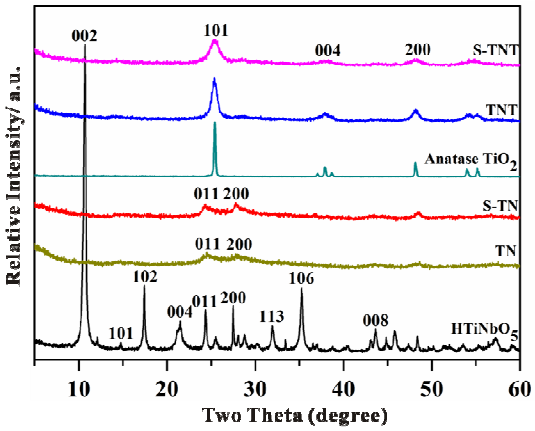

Fig. 3 XRD patterns of $HTiNbO_5$, TN, S-TN, commercial anatase TiO_2, TNT and S-TNT.

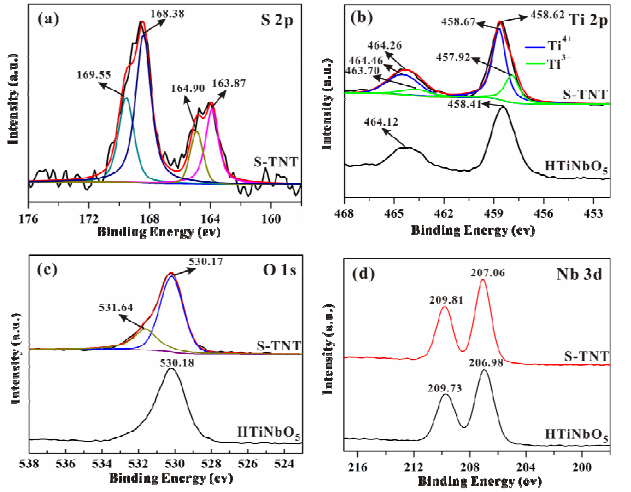

Fig. 4 XPS spectra of $HTiNbO_5$ and S-TNT (a) S 2p, (b) Ti 2p, (c) O 1s and (d) Nb 3d.

observed in S-TNT. By comparison, the resultant TNT without thiourea has almost the same characteristic diffraction peaks as S-TNT, indicating that the addition of thiourea has no significant effect on the product structure.

As we known, the anatase TiO_2 lattice is composed of the zigzag ribbon structure in which TiO_6 octahedra share four edges while both TiO_6 and NbO_6 octahedra were observed in $HTiNbO_5$.[39,40] The common structural features of TiO_6 octahedra in anatase TiO_2 and $HTiNbO_5$ reveal that anatase TiO_2 NPs can be deposited on the surface of $HTiNbO_5$ NSs to form the closely contacted interface, resulting in the formation of nano-heterojunction structure between two components so as to speed up the separation rate of photogenerated charge carriers.[35,41]

XPS and EPR studies

The chemical composition and states of atoms in $HTiNbO_5$ and S-TNT were further determined by XPS. It can be seen from Fig. S1 that the survey spectrum of S-TNT displays C, S, Ti, Nb and O elements. The carbon peak is attributed to adventitious hydrocarbon from the XPS instrument. It should be noted that the nitrogen peak does not appear in the XPS spectrum.

As shown in Fig. 4a, the S 2p state in S-TNT with a broadened peak at ~168 eV is attributed to the overlap of the split sublevels, $2p_{3/2}$ and $2p_{1/2}$ states. The amount of sulfur dopant was estimated to be ~2.01 at% in S-TNT by XPS. After fitting, two strong peaks, with a separation of ~1.20 eV by spin-orbit coupling,[42] are clearly observed at 168.38 and 169.55 eV, respectively. These two peaks indicate that the sulfur, in the form of S^{6+}, partially substitutes for Ti^{4+} in the lattice, leading to the formation of Ti−O−S bonds in S-TNT sample.[43] Thus, the cationic S-TNT sample is obtained, leading to a charge imbalance in the lattice of catalyst. The extra positive charge is probably neutralized by the adsorbed hydroxide ions (OH^-_{ads}), which could capture the photo-induced holes to form active groups typically as hydroxyl radicals ($^{\bullet}OH$).[43] These $^{\bullet}OH$ radicals are the main active species responsible for the degradation of organic pollutants. Furthermore, SO_4^{2-} groups were formed on the surface of S-TNT due to the heat treatment under atmospheric conditions.[44,45] Two possible coordination models between SO_4^{2-} and TiO_2 are shown in Fig. S2.[35] The surface-adsorbed SO_4^{2-} could act as the efficient electron trapping center to promote the separation of charge carriers.[45] In addition, it also exhibits two other primary peaks at 163.87 and 164.90 eV. The peak at 163.87 eV is attributed to the binding sulfurs in C−S_n−C (n=1 or 2) bonds and that at 164.9 eV to neutral S or S−S bond.[46,47] The −C−S−C− structure was reported to be an important factor for optimizing catalytic performance.[48] Combined with TEM and HRTEM results, it is reasonable to assume that S atoms are mainly incorporated into TiO_2 as the surface of $HTiNbO_5$ NSs is covered with anatase TiO_2 NPs and S doping proceeds gradually from exterior to interior.[34,41]

Ti 2p spectrum was performed to investigate the presence and chemical state of Ti^{3+} in S-TNT. As shown in Fig. 4b, two peaks at binding energies of 458.62 (Ti $2p_{3/2}$) and 464.26 eV (Ti $2p_{1/2}$) can be observed in the high resolution Ti 2p XPS spectrum of S-TNT. Compared with $HTiNbO_5$, the peaks of S-TNT are relatively broadened and show a shift towards higher binding energy, indicating that the chemical environment of Ti atoms in S-TNT is different from that in pristine $HTiNbO_5$. After fitting, two Ti 2p peaks of S-TNT are divided into four peaks at 457.92 (Ti^{3+} $2p_{3/2}$), 458.67 (Ti^{4+} $2p_{3/2}$), 463.70 (Ti^{3+} $2p_{1/2}$) and 464.46 eV (Ti^{4+} $2p_{1/2}$), indicating the presence of Ti^{3+} ions in S-TNT composite.[29] The formation of Ti^{3+} ions may be arisen from the decomposition of thiourea and TBAOH in the synthesis of S-TNT that consumes a large amount of oxygen and results in an oxygen deficient of oxygen vacancies.[49] Combined with the above results, it is reasonable to assume that Ti^{3+} ions are mainly introduced on the surface of $HTiNbO_5$ NSs. Generally, the existence of Ti^{3+} in TiO_2 indicated that the oxygen vacancies will be generated to maintain electrostatic balance.[50]

Two peaks are observed in the O 1s spectrum of S-TNT (Fig. 4c). The primary peak at a lower binding energy of 530.17 eV is attributed to the Ti−O−Ti bond while the secondary one at 531.64 eV is attributed to the surface OH^- groups.[29,51] The O 1s spectra illustrate that S-TNT has much more surface OH^- species. OH^- groups and adsorbed water can trap holes to form $^{\bullet}OH$ radicals which are capable of degrading organic pollutants in water.[52] Meanwhile, as shown in Fig. 4d, the two peaks of Nb 3d in S-TNT centered at 207.06 and 209.81 eV are quite similar to those in layered $HTiNbO_5$, indicating that the Nb atoms are chemically bound to oxygen rather than sulfur.

Room-temperature electron paramagnetic resonance (EPR)

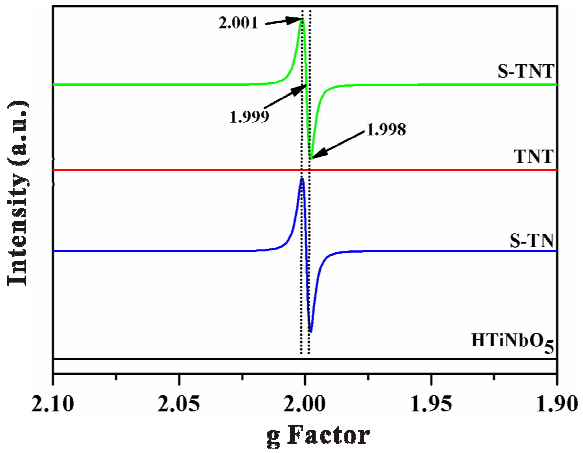

Fig. 5 Room-temperature EPR spectra of $HTiNbO_5$, S-TN, TNT and S-TNT.

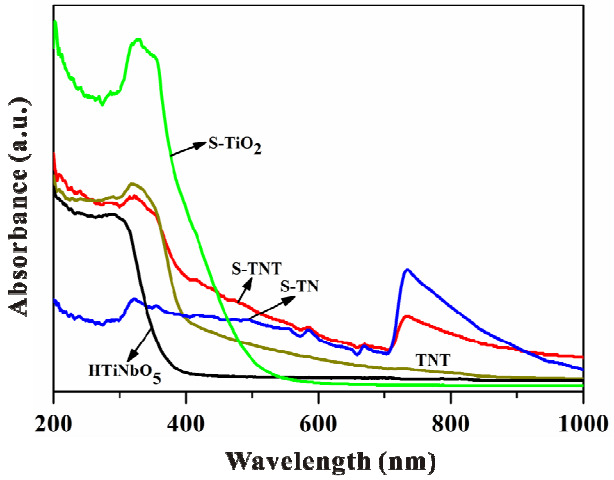

Fig. 6 Diffuse reflectance UV-visible spectra of $HTiNbO_5$, S-TN, $S\text{-}TiO_2$, TNT and S-TNT.

was conducted to further identify the presence of Ti^{3+} ions. As shown in Fig. 5, both $HTiNbO_5$ and TNT are EPR-silent, indicating that no localized unpaired electrons are present in these two samples. However, after S-doping, both S-TN and S-TNT show two peaks at g=2.001 and 1.998, which could be respectively attributed to oxygen vacancies and Ti^{3+} ions.[53] It indicates that the addition of thiourea plays an important role in the formation of Ti^{3+} ions. In addition, a broad signal at g=1.999, which is typical g values for a paramagnetic Ti^{3+} center, was observed for S-TN and S-TNT samples, attributing to Ti^{3+} on the surface.[29] Oxygen vacancy defects on the surface of S-TNT play an essential role in governing the adsorption of O_2 molecules, which interact with Ti^{3+} sites or act as electron scavengers.[50] In addition, the Ti^{3+} species from the removal of oxygen atoms would act as hole scavengers. These behaviors could retard the charge recombination and therefore improve the photocatalytic activity.

However, there are some contradictory interpretations concerning how the defects (Ti^{3+} and oxygen vacancies) affect the photoactivity. Chen *et al*. have succeeded in preparing black hydrogenated TiO_2 nanocrystals with excellent photocatalytic activity, attributing to the introduction of disorder and dopant into the surface of TiO_2.[54] However, a black TiO_2 with bulk defects has been prepared using high-temperature hydrogenation method, showing significantly poor photoactivity under sunlight.[55] This may be due to the fact that the formation of bulk vacancy defects could be counter-productive to improve the photocatalytic activity of TiO_2. Recently, it has been reported that improving ratio of surface to bulk defects could greatly improve the photocatalytic activity of TiO_2.[56, 57] Therefore, as a local state, the introduction of Ti^{3+} on the surface of TiO_2 can suppress the recombination of electron-hole pairs and promote charge separation, and thus to enhance the photocatalytic performance.[58]

UV-visible diffuse reflectance spectra

Fig. 6 shows UV-visible diffuse reflectance spectra of $HTiNbO_5$, S-TN, TNT, $S\text{-}TiO_2$ and S-TNT. Only an absorption band in the UV region is observed for $HTiNbO_5$, attributing to the band-to-band transition. After exfoliation and hybridization with TiO_2, the resulted TNT shows a much stronger absorption in the UV and visible light region. In addition, the bandgap energy of TNT is noticeably decreased to ~3.17 eV (Fig. S3a). Apart from the possible quantum size effect,[59] the main reason might be the formation of a nano-heterojunction between $HTiNbO_5$ NSs (*ca*. 3.20 eV) and anatase TiO_2 (*ca*. 3.20 eV) as a result of the electronic coupling between two components within the closely contacted interfaces.[35,60]

After S doping, the resulted S-TNT shows not only a significant absorption tail in the visible light region but also a relatively stronger absorption in the near-infrared region than the corresponding undoped TNT, and the bandgap energy is further decreased to ~3.08 eV (Fig. S3b). In addition, S-TNT and S-TN display the similar broad peak at ~733 nm, assigning to the formation of the oxygen vacancy level in the bandgap.[61] As the CB and VB potentials of $HTiNbO_5$ NSs were respectively −0.79 and 2.41 eV *vs*. NHE,[62] the energy potential of the local state in Ti^{3+}-doped $HTiNbO_5$ NSs was calculated to be −0.67 eV.

In addition, compared with $S\text{-}TiO_2$ and S-TN, S-TNT has a much stronger visible light response. The above results indicate that the formation of a nano-heterojunction and the incorporation of Ti^{3+} and S dopants successfully extend the light absorption from UV to visible and near-infrared region, resulting in a wider spectrum of solar absorption in S-TNT.[63]

Specific surface area and porosity

The surface area and pore structure of the resultant samples were studied by using N_2 adsorption-desorption isotherm measurements. As shown in Fig. 7a, $HTiNbO_5$ shows adsorption isotherms of type I according to BDDB classification and also no observable hysteresis in their desorption isotherm, indicating nonporous nature.[64] However, S-TN, TNT and S-TNT exhibit isotherms of type IV shape which is indicative of a typical mesoporous solid. TNT shows a type H3 hysteresis loop according to the IUPAC classification, suggesting that the sample is comprised of aggregates (loose assemblages) of plate-like particles.[41,65] By comparison, S-TNT presents a H2-type hysteresis loop which is typical for those materials with relatively uniform channel-like pores.[65] In addition, both TNT and S-TNT display only a weak adsorption of N_2 molecules in a low-pressure (p/p_0) region, indicating that micropores made little contribution to the nitrogen adsorption.[66]

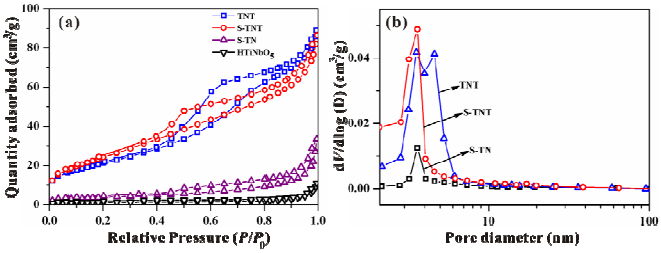

Fig. 7 N_2 adsorption and desorption isotherms (a) and pore size distribution curves (b) of $HTiNbO_5$, S-TN, TNT and S-TNT.

Table 1 Parameters obtained from N_2 adsorption-desorption measurements.

Sample	S_{BET}[a] (m^2/g)	V_t[b] (cm^3/g)	Pore sizec (nm)	Pore diameter (nm)
$HTiNbO_5$	4.4	0.018	9.6	—
S-TN	13.7	0.052	10.7	3.6
TNT	77.2	0.14	5.3	3.6, 4.6
S-TNT	90.1	0.13	5.0	3.6

[a] BET specific surface area calculated from the linear part of BET plot. [b] V_t= total pore volume taken from the volume of N_2 desorption at p/p_0 = 0.98.[c] The average pore diameter was estimated from the Barrett-Joyner-Halenda (BJH) formula.

The pore size distribution was analyzed from the desorption branch data based on the Barrett-Joyner-Halenda (BJH) method. As shown in Fig.7b, TNT has a binodal pore size distribution with centers at 3.6 and 4.6 nm while S-TNT shows only one pore size distribution center at 3.6 nm. The formation of mesopores is attributed to the exfoliation of ordered layered structure into NSs and then the formation of house-of-cards restacking structure of $HTiNbO_5$ NSs covered with TiO_2 NPs.[41]

As shown in Table 1, the BET specific surface area of $HTiNbO_5$ increases drastically upon exfoliation and hybridization. The BET specific surface area of the original $HTiNbO_5$ is only 4.4 m^2/g while that of TNT is greatly increased to 77.2 m^2/g. Compared with TNT, S-TNT shows a further improved BET surface area of 90.1 m^2/g. Thus, it can be concluded that exfoliation, hybridization and S-doping can efficiently fabricate catalyst with a greatly increased specific surface area and a mesoporous structure, leading to the formation of more reactive sites and thus being expected to enhance the photocatalytic performance for the degradation of organic pollutants.

Visible light photocatalytic performance

The visible light photocatalytic activities of the obtained samples were evaluated by the degradation of RhB aqueous solution. The photocatalytic degradation of RhB was monitored by the blank test. The result shows that the degradation of RhB is neglectable in the absence of photocatalyst under visible light irradiation. The photolysis of RhB over $HTiNbO_5$ and TN is very slow, and less than 17.0% and 29% of RhB are degraded under visible light irradiation within 160 min, respectively. The corresponding degradation is actually due to the surface adsorption and self-sensitization oxidation, as both $HTiNbO_5$ and TN have a large band-gap and cannot be activated by visible light.

Compared with TN, both S-TN and TNT show an enhanced visible light photocatalytic degradation rate of RhB, which is respectively due to S doping and the formation of nano-heterojunction between $HTiNbO_5$ NSs and TiO_2. Furthermore,

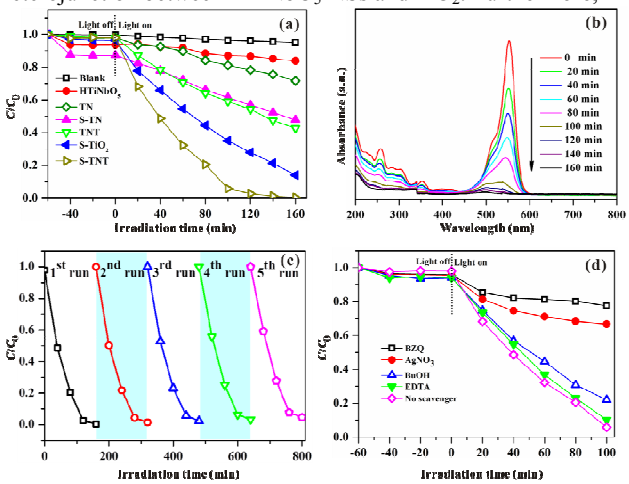

Fig. 8 (a) Visible light photocatalytic degradation rate of RhB solution over different samples, (b-c) UV-vis spectral change and photodegradation stability of RhB over S-TNT under visible light irradiation, and (d) time course of the photodegradation of RhB over S-TNT in the presence of various radicals scavengers.

after hybridization and S doping, a significantly enhanced photocatalytic performance is observed with S-TNT, showing the highest photocatalytic activity with 94.2% of RhB photodegraded in 100 min. It indicates that S doping essentially tunes the electric structure of TNT and thus further effectively enhances the photocatalytic performance. In addition, compared with S-TN and S-TiO_2, the enhanced photocatalytic activity of S-TNT also proves the importance of the formation of nano-heterojunction in enhancing the photocatalytic performance. Combined with the results from XPS, EPR and UV-vis spectra, the observed photobleaching over S-TNT under visible light irradiation should be mainly attributed to the oxidation photodegradation of dye molecules rather than the self-photosensitized oxidation or other reasons. To further identify the visible light photocatalytic activity of S-TNT, phenol that has no absorption in the visible light region was used as a probe molecule. It was found that phenol was also efficiently degraded over the composite photocatalyst under visible light irradiation (see Fig. S4), but it was hardly removed by $HTiNbO_5$ and TN under the same conditions.[67]

As shown in Fig. 8b, the rapid decrease in absorption intensity of all bands further shows that RhB is essentially degraded upon visible light irradiation in the presence of S-TNT composite. Moreover, although the composite was reused five times, it still exhibited a high photocatalytic activity (Fig. 8c). It indicates that S-TNT is a stable photocatalyst with a high activity for the removal of organic pollutants and does not photocorrode during the photocatalytic oxidation of pollutant molecules.

Based on the previously reported studies,[68,69] in order to understand the role of the photoexcited active species in the degradation of RhB dye, a succession of control experiments were performed. Different scavengers aiming for the trapped holes (h^+), e^-, $^{\bullet}OH$ and superoxide radicals ($O_2^{\bullet-}$), were added during the degradation process. Herein, EDTA, $AgNO_3$, BuOH and BZQ were used as scavengers of the trapped h^+, e^-, $^{\bullet}OH$ and $O_2^{\bullet-}$, respectively.

Fig. 8d presents the photocatalytic activity of S-TNT upon the

addition of different scavengers. The degradation efficiency was

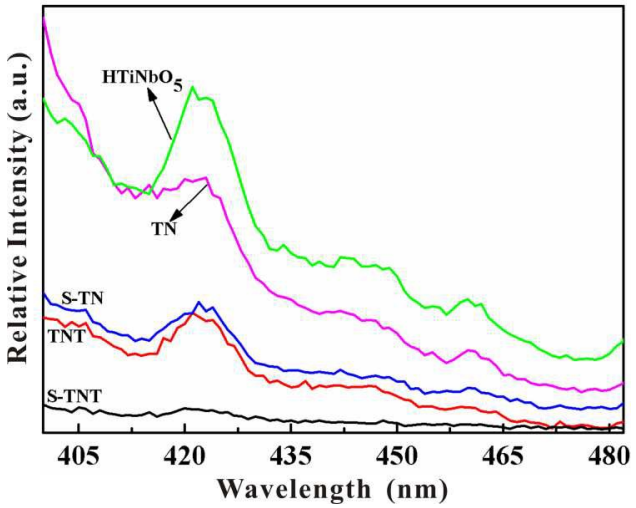

Fig. 9 PL spectra of $HTiNbO_5$, TN, S-TN, TNT and S-TNT with an excitation wavelength of 350 nm.

greatly decreased to 22.5%, 33.3%, 78.0% and 89.8% upon the addition of BZQ, $AgNO_3$, BuOH and EDTA, respectively. Thus, the role of active species in the degradation of RhB dye follows the order of $O_2^{\bullet-} > e^- > {}^{\bullet}OH > h^+$. This result indicates that h^+, e^-, ${}^{\bullet}OH$ and $O_2^{\bullet-}$ are all active species generated in S-TNT photocatalytic system. By comparison, it can be found that $O_2^{\bullet-}$ is the most crucial species while h^+ and ${}^{\bullet}OH$ are the least crucial ones during the photocatalytic degradation of RhB in the S-TNT system.

The PL technique is useful to reveal the migration, transfer and recombination process of photogenerated electron-hole pairs in semiconductors. A lower fluorescence emission intensity implies a lower electron-hole recombination rate and thus corresponds to a higher photocatalytic activity. In order to understand the role of TiO_2 hybridization and S doping in enhancing the visible light photocatalytic activity for RhB degradation, $HTiNbO_5$, TN, S-TN, TNT and S-TNT were characterized by PL with an excitation wavelength of 350 nm and the results are shown in Fig. 9.

The main emission peak is centered at ~422 nm for various samples, which can be ascribed to the band gap recombination of electron-hole pairs.[70,71] Layered $HTiNbO_5$ shows a strong PL emission peak, indicating that electrons and holes recombine rapidly. After exfoliation and calcination, the peak positions in the resulted TN are similar to those in pure $HTiNbO_5$ but the intensity of the main peak is reduced, indicating that TN has a low recombination rate of photogenerated electron-hole pairs. It confirms the importance of mesoporous structure in hindering the recombination of electrons and holes. Compared with TN, the PL intensity of S-TN is obviously reduced, indicating that S doping can efficiently suppress the recombination of photogenerated electron-hole pairs. On the other hand, after hybridization with TiO_2, it can also be observed that the PL intensity of the resulted TNT and S-TNT is further greatly diminished. These results indicate that exfoliation into NSs, hybridization with TiO_2 and S doping can effectively accelerate the separation of charge carriers.

Photocatalytic mechanism

Based on the above discussion, a possible mechanism for the photocatalytic degradation of RhB over S-TNT is proposed and

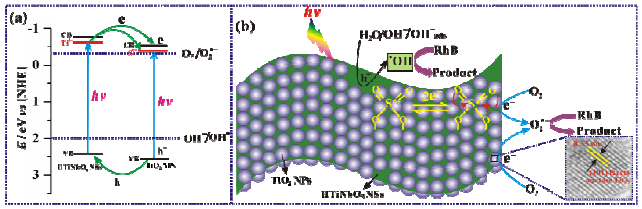

Fig. 10 (a) Energy levels of $HTiNbO_5$ NSs and anatase TiO_2 using a normal hydrogen electrode (NHE) as reference at pH 7. The potential of CB in TiO_2 was calculated from $E_{CB} = -0.12–0.059$ pH. (b) A schematic illustration of S-TNT composite catalyst for the photodegradation of RhB.

schematically shown in Fig. 10. The Ti^{3+} and oxygen vacancies form a local state below CB of $HTiNbO_5$ NSs, leading to the visible-light response. As the potentials of local state and VB of $HTiNbO_5$ NSs and those of S-doped anatase TiO_2 are −0.67 and 2.41 eV, and −0.41 and 2.67 eV, respectively, once irradiated under visible light source, a majority of electrons are able to jump from the VB to the local states formed by Ti^{3+} ions in $HTiNbO_5$ NSs, and then transfer to the CB (−0.53 eV *vs*. NHE) or intra-band-gap states created by the substitution of Ti^{4+} by S^{6+} in TiO_2 NPs due to the potential difference. The surface-adsorbed SO_4^{2-} could also act as the efficient electron trapping center to promote the separation of charge carriers. Then these excited-state electrons transfer to the surface of TiO_2 NPs and react with dissolved oxygen to generate the main active groups of $O_2^{\bullet-}$ as the standard redox potential of $O_2/O_2^{\bullet-}$ (−0.33 V *vs*. NHE) is more positive than the potential of CB or intra-band-gap states of TiO_2 NPs. In addition, the exposed anatase {101} facets could be acted as a possible reservoir of the photogenerated electrons, yielding a highly reactive surface for the reduction of O_2 to $O_2^{\bullet-}$. The formed $O_2^{\bullet-}$ then oxidizes RhB. This is consistent with the test results of the main oxidative species.

Meanwhile, since the VB edge potential of TiO_2 NPs (2.67 eV *vs*. NHE) is more positive than that of $HTiNbO_5$ NSs (2.41 eV *vs*. NHE), the holes at the VB of TiO_2 can transfer to the VB of $HTiNbO_5$ NSs. As the VB potential of $HTiNbO_5$ NSs is much more positive than the standard redox potential of ${}^{\bullet}OH/OH^-$ (1.99 V *vs*. NHE), the formed holes can react with OH^- groups or H_2O molecules to produce ${}^{\bullet}OH$ radicals. The formed ${}^{\bullet}OH$ radicals are able to oxidize the organic pollutant due to their high oxidative capacity. Therefore, the efficient separation of photogenerated electrons and holes can be achieved, leading to the improved utilization of charge carriers and ultimately the enhanced visible-light photocatalytic performance.

Conclusions

A facile exfoliation-reassembly-calcination method has been developed to prepare S-doped mesoporous $TiO_2/HTiNbO_5$ nanocomposite (S-TNT) in which anatase TiO_2 NPs with exposed {101} facets are deposited on the surface of $HTiNbO_5$ NSs, leading to the formation of nano-heterojunction structure between two components due to the common structural features of TiO_6 octahedra in anatase TiO_2 and $HTiNbO_5$. The resulted nanocomposite showed an excellent visible-light photocatalytic performance in degrading RhB and phenol solution due to the

following reasons. Firstly, the nano-heterojunction speeds up the separation rate of photogenerated charge carriers. Secondly, the partial substitution of Ti^{4+} by S^{6+} in S-TNT enhances the visible-light absorption and leads to the formation of considerable adsorbed hydroxide ions which could capture the photo-induced holes to form active hydroxyl radicals. In addition, with the formation of Ti−O−S bond, partial electrons can be transferred from S to O atoms. The electron-deficient S atoms might capture e^- and thus inhibits the recombination of photogenerated electron-hole pairs. Thirdly, the Ti^{3+} species from the removal of oxygen atoms and the associated oxygen vacancy defects on the surface of S-TNT could act as hole and electron scavengers, respectively. Besides, the surface-adsorbed SO_4^{2-} could also act as the efficient electron trapping center to promote the separation of charge carriers. Fourthly, the exposed anatase {101} facets could be acted as a possible reservoir of the photogenerated electrons, yielding a highly reactive surface for the reduction of O_2 to $O_2^{\bullet-}$ and thus the decrease of recombination probability of electron-hole pairs. Finally, the resulted nanocomposite shows a much larger specific surface area and rich mesoporosity, leading to the formation of more reactive sites, and thus further improving the photocatalytic performance.

The present work may provide an important indication of how to construct novel visible-light photocatalysts through an integration of hybridization, doping and morphology engineering.

Acknowledgements

The authors greatly appreciate the financial support of Specialized Research Fund for the Doctoral Program of Higher Education (SRFDP, 20130091110010), National Science Fund for Talent Training in Basic Science (No. J1103310), National Basic Research Program (973 Project) (No. 2009CB623504) and the Modern Analysis Center of Nanjing University. Thanks also go to Prof. Yongfa Zhu from Tsinghua University for his helpful suggestions.

Notes and references

[a] *Key Laboratory of Mesoscopic Chemistry of MOE, School of Chemistry and Chemical Engineering, Nanjing University, Nanjing 210023, P. R. China. E-mail: whou@nju.edu.cn*

[b] *School of Materials Engineering, Yancheng Institute of Technology, Yancheng, 224051, P. R. China.*

[c] *Department of Applied Chemistry, College of Science, Nanjing Tech University, Nanjing 211816, P. R. China.*

† Electronic Supplementary Information (ESI) available: [details of XPS, Two possible structures of the surface-adsorbed sulfate groups in S-TNT and The relationship bwtween $(Ahv)^2$ and photo energy (hv) of TNT and S-TNT]. See DOI: 10.1039/b000000x/

1 R. Asahi, T. Morikawa, H. Irie and T. Ohwaki, *Chem. Rev.,* 2014, **114**, 9824-9852.
2 S.W. Zhang, J.X. Li, X.K. Wang, Y.S. Huang, M.Y. Zeng and J.Z. Xu, *J. Mater. Chem. A*, 2015, **3**, 10119-10126.
3 T. Hisatomi, J. Kubota and K. Domen, *Chem. Soc. Rev*., 2014, **43**, 7520-7535.
4 F. Fresno, R. Portela, S. Suárez and J.M. Coronada, *J. Mater. Chem. A*, 2014, **2**, 2863-2884.
5 A. Kudo and Y. Miseki, *Chem. Soc. Rev.*, 2009, **38**, 253-278.
6 K. Shimura and H. Yoshida, *Energ. Environ. Sci.*, 2011, **4,** 2467-2481.
7 S.P. Wang, C.J. Li, T. Wang, P. Zhang, A. Li and J.L. Gong, *J. Mater. Chem. A*, 2014, **2**, 2885-2890.
8 C.C. Chen, W.H. Ma and J.C. Zhao, *Chem. Soc. Rev*., 2010, **39**, 4206-4219.
9 J.J. Wang, Z.Y. Guan, J. Huang, Q.X. Li and J.L. Yang, *J. Mater. Chem. A*, 2014, **2**, 7960-7966.
10 S. Tonda, S. Kumar, S. Kandula and V. Shanker, *J. Mater. Chem. A*, 2014, **2**, 6772-6780.
11 M. Dahl, Y.D. Liu and Y.D. Yin, *Chem. Rev*., 2014, **114,** 9853-9889.
12 X.B. Chen, L. Liu and F.Q. Huang, *Chem. Soc. Rev.*, 2015, **44,** 1861-1885.
13 L.X. Sang, Y.X. Zhao and C. Burda, *Chem. Rev*., 2014, **114**, 9283-9318.
14 L. Zhang, D.E. Jing, X.L. She, H.W. Liu, D.J. Yang, Y. Lu, J. Li, Z. F. Zheng and L.J. Guo, *J. Mater. Chem. A*, 2014, **2**, 2071-2078.
15 P. Miro, M. Audiffred and T. Heine, *Chem. Soc. Rev.*, 2014, **43,** 6537-6554.
16 C.M. Li, M. Wei, D.G. Evans and X. Duan, *Small*, 2014, **10**, 4469-4486.
17 Q. Wang and D. O'Hare, *Chem. Rev.*, 2012, **112**, 4124-4155.
18 X. Zong and L.Z. Wang, *J. Photochem. Photobiol. C*, 2014, **18**, 32-49.
19 L.Z. Wang and T. Sasaki, *Chem. Rev*., 2014, **114**, 9455-9486.
20 A. Takagaki, C. Tagusagawa, S. Hayashi, M. Hara and K. Domen, *Energ. Environ. Sci*., 2010, **3**, 82-93.
21 Y.F. Sun, S. Gao, F.C. Lei and Y. Xie, *Chem. Soc. Rev*., 2015, **44**, 623-636.
22 L.H. Zhang, C.H. Hu, J.F. Zhang, L.Y. Cheng, Z. Zhai, J. Chen, W.P. Ding and W.H. Hou, *Chem. Commun*., 2013, **49**, 7507-7509.
23 X.R. Fan, B.Z. Lin, H. Liu, L.W. He, Y.L. Chen and B.F. Gao, *Int. J. Hydrogen Energ.*, 2013, **38,** 832-839.
24 Z.W. Zhao, Y.J. Sun and F. Dong, *Nanoscale*, 2015, **7,** 15-37.
25 S.W. Cao, J.X. Low, J.G. Yu and M. Jaroniec, *Adv. Mater.*, 2015, **27**, 2150-2176.
26 P. Zhang, J.J. Zhang and J.L. Gong, *Chem. Soc. Rev.,* 2014, **43**, 4395-4422.
27 J.J. Guo, S.X. Ouyang, P. Li, Y.J. Zhang, T. Kako and J.H. Ye, *Appl. Catal., B: Environ*., 2013, **134–135**, 286-292.
28 W. Zhou, W. Li, J.Q. Wang, Y. Qu, Y. Yang, Y. Xie, K.F. Zhang, L. Wang, H.G. Fu and D.Y. Zhao, *J. Am. Chem. Soc.*, 2014, **136**, 9280-9283.
29 J.C. Huo, Y.J. Hu, H. Jiang and C.Z. Li, *Nanoscale*, 2014, **6**, 9078-9084.
30 M. Kitano and M. Hara, *J. Mater. Chem*., 2010, **20**, 627-641.
31 J. Tian, Z.H. Zhao, A. Kumar, R.I. Boughton and H. Liu, *Chem. Soc. Rev.*, 2014, **43**, 6920-6937.
32 G. Liu, H.G. Yang, J. Pan, Y.Q. Yang, G.Q. Lu and H.M. Cheng, *Chem. Rev.*, 2014, **114**, 9559-9612.
33 E. Grabowska, M. Diak, M. Marchelek and A. Zaleska, *Appl. Catal., B: Environ.*, 2014, **156–157**, 213-235.
34 C. Liu, T. Sun, L. Wu, J.Y. Liang, Q.J. Huang, J. Chen and W.H. Hou, *Appl. Catal., B: Environ.,* 2015, **170–171**, 17-24.
35 C. Liu, J.Y. Liang, R.R. Han, Y.Z. Wang, J. Zhao, Q.J. Huang, J. Chen and W.H. Hou, *Phys. Chem. Chem. Phys.*, 2015, **17**, 15165-15172.
36 C. Liu, L. Wu, J. Chen, J.Y. Liang, C.S. Li, H.M. Ji and W.H. Hou, *Phys. Chem. Chem. Phys.*, 2014, **16**, 13409-13417.
37 M. D'Arienzo, J. Carbajo, A. Bahamonde, M. Crippa, S. Polizzi, R. Scotti, L. Wahba and F. Morazzoni, *J. Am. Chem. Soc*., 2011, **133**, 17652-17661.
38 Z. Zhai, Y.C. Huang, L. Xu, X.Y. Yang, C.H. Hu, L.H. Zhang, Y.N. Fan and W.H. Hou, *Nano Res.*, 2011, **4**, 635-647.
39 J.K. Burdett, T. Hughbanks, G.J. Miller, J.W. Richardson and J.V. Smith, *J. Am. Chem. Soc.*, 1987, **109,** 3639-3646.
40 Z. Zhai, X.Y. Yang, L. Xu, C.H. Hu, L.H. Zhang, W.H. Hou and Y.N. Fan, *Nanoscale*, 2012, **4**, 547-556.
41 Z. Zhai, C.H. Hu, X.Y. Yang, L.H. Zhang, C. Liu, Y.N. Fan and W.H. Hou, *J. Mater. Chem.*, 2012, **22**, 19122-19131.
42 B.J. Lindberg and K. Hamrin, *Acta Chem. Scand*., 1970, **24**, 3661-3671.

43 J.C. Yu, W. Ho, J. Yu, H. Yip, P.K. Wong and J.C. Zhao, *Environ. Sci. Technol.*, 2005, **39**, 1175-1179.

44 D. Ma, Y.J. Xin, M.C. Gao and J. Wu, *Appl. Catal., B: Environ.*, 2014, **147**, 49-57.

45 P.V.R.K. Ramacharyulu, J. Praveen Kumar, G.K. Prasad and B. Sreedhar, *Mater. Chem. Phys.*, 2014, **148**, 692-698.

46 H. Gao, Z. Liu, L. Song, W.H. Guo, W. Gao, L.J. Ci, A. Rao, W.J. Quan, R. Vajtai and P.M. Ajayan, Nanotechnology, 2012, **23** 275605.

47 J.P. Paraknowitsch, B. Wienert, Y.J. Zhang and A. Thomas, *Chem. Eur. J.*, 2012, **18**, 15416-15423.

48 H. Wang, X.J. Bo, Y.F. Zhang and L.P. Guo, *Electrochim. Acta*, 2013, **108**, 404-411.

49 C.H. Ma, J. Zhou, H.Y. Zhu, W.W. Yang, J.G. Liu, Y. Wang and Z.G. Zou, *ACS Appl. Mater. Inter.*, 2015, **7**, 14628-14637.

50 X.D. Jiang, Y.P. Zhang, J. Jiang, Y.S. Rong, Y.C. Wang, Y.C. Wu and C.X. Pan, *J. Phys. Chem. C*, 2012, **116,** 22619-22624.

51 K. Li, S.M. Gao, Q.Y. Wang, H. Xu, Z.Y. Wang, B.B. Huang, Y. Dai and J. Lu, *ACS Appl. Mater. Inter.*, 2015, **7**, 9023-9030.

52 G. Liu, X.X. Yan, Z.G. Chen, X.W. Wang, L.Z. Wang, G.Q. Lu and H.M. Cheng, *J. Mater. Chem.*, 2009, **19**, 6590-6596.

53 W.Z. Fang, M.Y. Xing and J.L. Zhang, *Appl. Catal., B: Environ.*, 2014, **160–161,** 240-246.

54 X.B. Chen, L. Liu, P.Y. Yu and S.S. Mao, Science, 2011, **331,** 746-750.

55 T. Leshuk, R. Parviz, P. Everett, H. Krishnakumar, R.A. Varin and F. Gu, *ACS Appl. Mater. Inter.*, 2013, **5**, 1892-1895.

56 M. Kong, Y.Z. Li, X. Chen, T.T. Tian, P.F. Fang, F. Zheng and X.J. Zhao, *J. Am. Chem. Soc.*, 2011, **133,** 16414-16417.

57 X.M. Yu, B. Kim and Y.K. Kim, *ACS Catal*., 2013, **3**, 2479-2486.

58 S.H. Szczepankiewicz, J.A. Moss and M.R. Hoffmann, *J. Phys. Chem. B*, 2002, **106,** 2922-2927.

59 Z.J. Chen, B.Z. Lin, Y.L. Chen, K.Z. Zhang, B. Li and H. Zhu, *J. Phys. Chem. Solids*, 2010, **71**, 841-847.

60 G.H. Du, Y. Yu, Q. Chen, R.H. Wang, W. Zhou and L.M. Peng, *Chem. Phys. Lett.*, 2003, **377,** 445-448.

61 G.S. Li, Z.C. Lian, X. Li, Y.Y. Xu, W.C. Wang, D.Q. Zhang, F.H. Tian and H.X. Li, *J. Mater. Chem. A*, 2015, **3**, 3748-3756.

62 O. Zhang, B.Z. Lin, Y.L. Chen, B.F. Gao, L.M. Fu and B. Li, *Electrochim. Acta*, 2012, **81**, 74-82.

63 C.Y. Yang, Z. Wang, T.Q. Lin, H. Yin, X. Lü, D.Y. Wan, T. Xu, C. Zheng, J.F. Lin, F.Q. Huang, X.M. Xie and M.H. Jiang, *J. Am. Chem. Soc.*, 2013, **135**, 17831-17838.

64 S.J. Gregg and K.S.W. Sing, Adsorption, Surface Area and Porosity. 2nd Ed, Academic Press, 1982.

65 M. Kruk and M. Jaroniec, *Chem. Mater.*, 2001, **13**, 3169-3183.

66 T.W. Kim, H.W. Ha, M.J. Paek, S.H. Hyun, I.H. Baek, J.H. Choy and S.J. Hwang, *J. Phys. Chem. C*, 2008, **112,** 14853-14862.

67 Y. Mi, M. Zhou, L.Y. Wen, HP. Zhao and Y. Lei, *Dalton Trans*., 2014, **43**, 9549-9556.

68 H.W. Huang, K. Liu, Y.L. Zhang, K. Chen, Y.H. Zhang and N. Tian, *RSC Adv.*, 2014, **4**, 49386-49394.

69 Y.X. Yang, W. Guo, Y.N. Guo, Y.H. Zhao, X. Yuan and Y.H. Guo, *J. Hazard. Mater.*, 2014, **271,** 150-159.

70 Q.J. Xiang, J.G. Yu and M. Jaroniec, *J. Phys. Chem. C*, 2011, **115**, 7355-7363.

71 W.G. Tu, Y. Zhou, Q. Liu, S.C. Yan, S.S. Bao, X.Y. Wang, M. Xiao and Z.G. Zou, *Adv. Funct. Mater.*, 2013, **23**, 1743-1749.